

# An exact analytic treatment of propagating mass accretion rate fluctuations in X-ray binaries

Adam Ingram<sup>★</sup> and Michiel van der Klis

*Astronomical Institute, Anton Pannekoek, University of Amsterdam, Science Park 904, 1098 XH Amsterdam, the Netherlands*

Accepted 2013 June 17. Received 2013 June 15; in original form 2013 June 12

## ABSTRACT

Many statistical properties of the aperiodic variability observed in X-ray radiation from accreting compact objects can be naturally explained by the propagating fluctuations model. This considers variations in mass accretion rate to be stirred up throughout the accretion flow. Variations from the outer regions of the accretion flow will propagate towards the central object, modulating the variations from the inner regions and eventually modulating the radiation, giving rise to the observed linear rms–flux relation and also Fourier frequency-dependent time lags. Previous treatments of this model have relied on computationally intensive Monte Carlo simulations which can only yield an *estimate* of statistical properties such as the power spectrum. Here, we find *exact* and *analytic* expressions for the power spectrum and lag spectrum predicted by the *same* model. We use our calculation to fit the model of Ingram & Done to a power spectrum of XTE J1550–564. The result we present here will apply to any treatment of the propagating fluctuations model and thus provides a very powerful tool for future theoretical modelling.

**Key words:** accretion, accretion discs – X-rays: binaries.

## 1 INTRODUCTION

Over the last 20 yr, mainly thanks to the *Rossi X-ray Timing Explorer (RXTE)*, a detailed phenomenology of the spectral and timing properties of accreting black hole binaries (BHBs) has emerged in the literature (see e.g. Homan et al. 2001; van der Klis 2006; Done, Gierliński & Kubota 2007; Belloni 2010). A typical transient BHB in outburst runs through three spectral states classified as the hard, intermediate and soft states. The hard state spectrum is dominated by a hard (photon index  $\Gamma \approx 1.7$ ) power law with a comparatively weak contribution from an optically thick accretion disc. A softening of the power law ( $\Gamma \approx 1.7$ –2.4) and an increased contribution from the disc mark the transition through the intermediate state, with the disc becoming completely dominant in the soft state. In addition to direct disc emission, reflection features are also observed including an iron  $K\alpha$  emission line. The direct disc emission is well understood as a multitemperature blackbody (Novikov & Thorne 1973; Shakura & Sunyaev 1973) and, although there is still disagreement about the exact nature of the accretion geometry, it is generally accepted that the power law originates from Compton upscattering of cool ‘seed’ photons (most likely supplied by the accretion disc, although it is likely that synchrotron radiation from the flow is important in the hard state; Sobolewska et al. 2011; Skipper, McHardy & Maccarone 2013) by hot electrons in some optically thin (optical depth  $\tau \approx 1$ ) cloud (Thorne & Price 1975; Sunyaev

& Truemper 1979). The position and nature of this cloud are the source of much debate but it is often interpreted as an optically thin accretion flow (hereafter *the flow* as opposed to *the disc* surrounding it) formed from disc evaporation inside some truncation radius,  $r_o$  (the *truncated disc model*; Ichimaru 1977; Esin, McClintock & Narayan 1997; Gilfanov, Churazov & Revnivtsev 2000; Done et al. 2007; Gilfanov 2010). In the hard state,  $r_o$  is large and thus only a small luminosity of cool disc photons irradiate the flow, giving rise to a hard spectrum with only a weak direct contribution from the disc and also weak reflection features. As  $r_o$  moves inward, a greater luminosity of disc photons cools the flow, thus softening the power law and also increasing the contribution to the observed spectrum from direct disc emission. The fraction of the power-law emission reflected back into the line of sight from the disc also naturally increases in this geometry, as is observed (e.g. Gilfanov 2010).

The timing properties of BHBs evolve in a manner tightly correlated with the spectral evolution. The observed fast ( $\sim 100$ –0.01 s) variability can be characterized by studying the power spectrum of the flux time series. Typically the hard state power spectrum consists of aperiodic broad-band noise plus a narrower (type C) quasi-periodic oscillation (QPO) with associated harmonics. Phenomenological modelling using multiple Lorentzian components reveals that all characteristic frequencies associated with the power spectrum<sup>1</sup> *increase* as the source transitions from hard to soft state,

<sup>1</sup> The characteristic frequency is defined as  $\nu_{\text{peak}}^2 = \Delta\nu^2 + \nu_0^2$ , where  $\Delta\nu$  and  $\nu_0$  are the width (half width at half-maximum) and centroid, respectively.

<sup>★</sup> E-mail: a.r.ingram@uva.nl

with the QPO becoming increasingly prominent before the emission becomes stable in the soft state (Churazov, Gilfanov & Revnivtsev 2001; Belloni, Psaltis & van der Klis 2002, and references therein). In particular, the characteristic frequency of the lowest frequency Lorentzian in the fit  $\nu_b$ , often referred to as the low-frequency break, correlates with the QPO frequency (*the QPO–break relation*; Wijnands & van der Klis 1999; also see Klein-Wolt & van der Klis 2008). Another fundamental property of the emission which cannot be probed using the power spectrum is the *linear* relation between the absolute rms variability integrated over any two time-scales and the flux averaged over any longer time-scale (*the rms–flux relation*; Uttley & McHardy 2001; Heil, Vaughan & Uttley 2012). The observation that this relation seems to hold over all time-scales rules out previously popular shot noise models (Terrell 1972; Weisskopf, Kahn & Sutherland 1975), since the rms and flux from a series of unrelated flares (or shots) with some shot length drawn from a probability distribution cannot be linearly related on time-scales longer than the shot length (Uttley, McHardy & Vaughan 2005). The variability is also highly coherent across a broad range of energy bands (Vaughan & Nowak 1997; Nowak et al. 1999) and a cross-spectral analysis reveals Fourier-frequency-dependent time lags between energy bands, with hard lagging soft by a greater amount for smaller Fourier frequencies (Miyamoto & Kitamoto 1989; Nowak et al. 1999).

Although the physical processes behind the timing properties are very poorly understood in comparison to the spectral properties, the broad-band noise is increasingly often attributed to propagating fluctuations in mass accretion rate (Lyubarskii 1997; Kotov, Churazov & Gilfanov 2001; Arévalo & Uttley 2006). In this picture, fluctuations stirred up far from the black hole modulate the mass accretion rate closer to the black hole. Since this is a multiplicative process, the emitted flux is naturally predicted to display a linear rms–flux relation (Arévalo & Uttley 2006). If a harder spectrum is emitted from the inner regions compared with the outer regions, this also naturally gives rise to the time lags with fluctuations imprinted in the soft band being emitted in the hard band only after some propagation time (Kotov et al. 2001; Arévalo & Uttley 2006).

In this model, the power spectral shape of the broad-band noise depends on both the noise generating process *and* the response of the accretion flow. The magnetorotational instability (MRI; Hawley & Balbus 1991; Balbus & Hawley 1998) is most likely the underlying noise generator, which (very approximately) produces a white noise of variability everywhere in the flow due to magnetic field lines interacting with differentially rotating gas. The response of a Keplerian accretion flow to a white noise of intrinsic fluctuations is governed by the diffusion equation (Lynden-Bell & Pringle 1974; Pringle 1981; Lyubarskii 1997; Churazov et al. 2001; Frank, King & Raine 2002). Solving this for a  $\delta$ -function perturbation (i.e. calculating the Green’s function) yields that the power spectrum of the mass accretion rate far from the radius where the noise originated is approximately a zero-centred Lorentzian with width  $1/t_{\text{visc}}(r)$ , where  $t_{\text{visc}}(r)$  is the local viscous time-scale (Lyubarskii 1997; Pringle 1981).<sup>2</sup> Since  $t_{\text{visc}}(r)$  is *longer* for larger  $r$ , this implies that variability on different time-scales predominantly originates from different regions of the accretion flow with higher frequencies coming from closer to the black hole. Churazov et al. (2001), motivated by the stability of the disc-dominated soft state in Cygnus X-1, proposed that variability is only generated in the flow. In this

stable disc/noisy flow picture, the low-frequency break  $\nu_b \approx 1/t_{\text{visc}}(r_o)$  is naturally predicted to increase as  $r_o$  moves in. Although subsequent observations of disc variability in the hard state of GX 339–4 and SWIFT J1753.5–0127 (Wilkinson & Uttley 2009; Uttley et al. 2011) suggest this picture is overly simplistic, it forms the starting point for the power spectral model we defined in Ingram & Done (2011, 2012a; hereafter ID11 and ID12), although we stress that disc variability must eventually be taken into account.

There is even more uncertainty surrounding the physical origin of the QPO, with many mechanisms suggested in the literature (Marković & Lamb 1998; Stella & Vietri 1998; Tagger & Pellat 1999; Titarchuk & Osherovich 1999; Fragile, Mathews & Wilson 2001; Wagoner, Silbergleit & Ortega-Rodríguez 2001; Schnittman 2005; Schnittman, Homan & Miller 2006; Cabanac et al. 2010). A popular class of QPO model considers characteristic orbital frequencies at  $r_o$ . In general relativity, frame dragging due to the rotation of a massive object drags the orbital plane of a test mass around the spin axis of the massive object, giving rise to precession if the two spin axes are misaligned (Lense–Thirring precession). Stella & Vietri (1998) noted that the observed range of QPO frequencies ( $\sim 0.1$ –10 Hz) matches the Lense–Thirring precession frequency of a test mass orbiting at  $r_o$  for a range of  $r_o$  considered reasonable from spectral fitting ( $\sim 60$ –6  $R_g$ , where  $R_g = GM/c^2$ ). After Fragile et al. (2007) showed in a general relativistic magnetohydrodynamic (GRMHD) simulation that an optically thin accretion flow misaligned with the black hole spin axis can precess as a solid body, Ingram, Done & Fragile (2009) suggested that the QPO arises from precession of the entire inner flow. This turns out to be a very attractive model which can predict the correct range of QPO frequencies for BHBs (Ingram et al. 2009) and also atoll sources (low-mass accretion rate neutron star binaries; Ingram & Done 2010). It also naturally explains the apparent inclination dependence of QPO strength (Schnittman et al. 2006) as well as a number of other more subtle QPO properties (Sobolewska & Życki 2006; Heil, Vaughan & Uttley 2011; ID11; Ingram & Done 2012b). However in Altamirano et al. (2012), we showed that the  $\sim 35$ –50 Hz QPO in the 11 Hz pulsar in the globular cluster Terzan 5 cannot possibly originate from Lense–Thirring precession. This source displays a QPO–break relation consistent with other Z-sources, implying that the low-frequency QPOs in Z-sources (horizontal branch oscillations) do not originate from Lense–Thirring precession. Since Z-sources display a somewhat different QPO–break relation to atolls and BHBs (following a track a factor of  $\sim 2$  higher in QPO frequency and displaying a turnover at  $\nu_b \sim 10$  Hz if data from Terzan 5 X-2 and Sco X-1 are considered), we cannot rule out the model in general from this observation.

ID11 and ID12 defined and developed a power spectral model which combines propagating mass accretion rate fluctuations with Lense–Thirring precession. The algorithm of Timmer & Koenig (1995, hereafter TK95; also see Davies & Harte 1987) was used to simulate mass accretion rate fluctuations with a random phase in order to *estimate* the power spectrum. This led to two major disadvantages: (1) the power spectrum calculated in this way is inexact giving rise to errors associated with the model; (2) the simulation is *very* computationally intensive, meaning it took weeks to find a local minimum in  $\chi^2$  and full error calculations were not feasible. In this paper, we describe how the same calculation can be done analytically. We show that this gives the same results as the simulation and test a slightly modified version of the model against a data set previously considered in ID12. The new calculation is extremely fast, meaning we can now fully explore parameter space. We also discuss how our result here can be combined with more

<sup>2</sup> Since the Green’s function is  $\sim e^{t/t_{\text{visc}}(r)}$  and the Fourier transform of an exponential is a Lorentzian.

sophisticated physical assumptions in future work to define more realistic analytic models of the accretion flow.

## 2 A RANDOM WALK ON THE COMPLEX PLANE

In the propagating fluctuations model, the mass accretion rate at some point in the flow is the product of many stochastic time series. Previous treatments of this model have involved simulating time series before estimating the power spectrum of their product by averaging over many realizations. In this section, we show that the power spectrum of this product can be calculated analytically. We first define important quantities before considering multiplying two, followed by an arbitrary number of time series.

### 2.1 Definitions

We define the discrete Fourier transform (DFT) of a time series  $a_k$ , evaluated at time  $k \, dt$  with  $k = 1, \dots, N$ , as

$$A_j = \frac{1}{N} \sum_{k=1}^N a_k e^{i2\pi jk/N} \quad (1)$$

(see e.g. Oppenheim & Schaffer 1975; van der Klis 1989; Press et al. 1992). Here,  $A_j$  is evaluated at frequency  $\nu_j = j \, d\nu = j/(Ndt)$ , where  $j = -N/2 + 1, \dots, N/2$ . From this it follows that the inverse transform is

$$a_k = \sum_{j=-N/2+1}^{N/2} A_j e^{-i2\pi jk/N}. \quad (2)$$

Since we are always considering  $a_k$  to be some physical signal, it must be real and thus its DFT is complex conjugate symmetric ( $A_{-j} = A_j^*$ ) and its periodogram,  $|A_j|^2$  (again with  $j = -N/2 + 1, \dots, N/2$ ), is symmetric about  $j = 0$  ( $|A_{-j}|^2 = |A_j|^2$ ). Hereafter, we refer to  $j = 0$  and  $j \neq 0$  terms, respectively, as the DC and AC components (standing for direct and alternating current). Under these definitions, a time series with mean  $\mu$ , variance  $\sigma^2$  and duration  $T = N \, dt$ , has a DC component  $A_0 = \mu$  and AC components obeying the following form of Parseval's theorem:

$$\sum_{j=1}^{N/2} |A_j|^2 \, d\nu - \frac{|A_{N/2}|^2 \, d\nu}{2} = \frac{\sigma^2}{2T}. \quad (3)$$

For plots in this paper, we re-normalize the periodogram by a factor  $2T$  or  $2T/\mu^2$  such that its integral over all positive frequencies is approximately  $\sigma^2$  or  $(\sigma/\mu)^2$ . From equation (3), we see that this approximation becomes very good for large  $N$ .

In our application,  $a_k$  is stochastic and so represents a particular realization of an underlying process. The periodogram,  $|A_j|^2$ , represents the power spectrum of the *realization*. The average periodogram,  $\langle |A_j|^2 \rangle$ , provides an estimate for the power spectrum of the *process*,  $|A(\nu_j)|^2$ , which becomes exact when the averaging is over infinite realizations. Hereafter, we adopt the convention that the *power spectrum* always refers to the process and the *periodogram* always refers to the realization. The TK95 algorithm generates a realization of the process with power spectrum  $|A(\nu_j)|^2$ . It generates a real time series  $a_k$  as the inverse DFT of the complex conjugate symmetric series  $A_j$ , which obeys

$$\langle |A_j|^2 \rangle = \langle \Re A_j^2 \rangle + \langle \Im A_j^2 \rangle = |A(\nu_j)|^2. \quad (4)$$

For  $j = 1, \dots, N/2 - 1$ , the real and imaginary parts of  $A_j$  are random variables chosen from a Gaussian distribution with

zero mean and the same variance which we can see from equation (4) must be equal to  $|A(\nu_j)|^2/2$ . Finally,  $\Re A_{-j} = \Re A_j$  and  $\Im A_{-j} = -\Im A_j$  to ensure  $a_k$  is real. These conditions ensure that the phase  $\phi_j$  is uniformly random on the interval  $-\pi < \phi_j \leq \pi$  for these frequencies. For the Nyquist frequency ( $j = N/2$ ),  $A_j$  is always real. Consequently, the variance of the zero-mean Gaussian distribution from which  $\Re A_j$  is chosen must, from equation (4), be equal to  $|A(\nu_j)|^2$ . Even though the Nyquist component is always real, its phase is still random, either taking the value  $\phi_{N/2} = 0$  or  $\phi_{N/2} = \pi$ , with an equal chance of each eventuality. We give the time series a mean, and thus DC component, of  $\mu_a$ .

Finally, we also define the cross-spectrum between two real time series  $a_k$  and  $b_k$  as  $C(\nu_j) = A(\nu_j)^* B(\nu_j)$  with  $j = -N/2 + 1, \dots, N/2$ . In direct analogy to our definition of the power spectrum, we adopt the convention that this is a property of the process as opposed to a particular realization and is given by  $C(\nu_j) = \langle A_j^* B_j \rangle$ , with the property  $C(\nu_{-j}) = C(\nu_j)^*$ . Note that, although the power and cross-spectra are defined for  $j < 0$ , their symmetry about  $j = 0$  ensures that the negative frequency components contain no extra information.

### 2.2 Multiplying two time series

Let us now take two time series generated via the TK95 method,  $a_k$  and  $b_k$ , and multiply them together to get  $x_k = a_k b_k$ . The DFT of  $x_k$  is

$$X_j = \sum_{k=-N/2+1}^{N/2} A_{j-k} B_k. \quad (5)$$

This is the convolution theorem. Since  $A_{j-k}$  is periodic on the interval  $j - k = -N/2 + 1, \dots, N/2$ , we can add or subtract  $N$  to the index of  $A$  in order to keep it in the desired interval. We wish to calculate the power spectrum of  $x_k$  without simulating. Since, for each value of  $j$ ,  $s_{jk} = A_{j-k} B_k$  is a series of  $N$  random variables, each with well defined average amplitude and random phase, equation (5) represents a random walk on the complex plane.<sup>3</sup>  $X_j$  is thus the final position on the complex plane after  $N$  steps have been taken. It follows that  $|X_j|$  is the distance covered by the random walk. Fig. 1 shows an example of this with all  $|s_{jk}| = 1$ .

We see from equation (5) that  $|X_j|^2$  is given by a sum over all  $|s_{jk}|^2$  plus many cross terms. If we average  $|X_j|^2$  over infinite realizations, all of these cross terms go to zero since the  $s_{jk}$  terms are uncorrelated with one another and we arrive at a well-known theorem for the length of a Gaussian random walk (see e.g. Weiss 1994):

$$\langle |X_j|^2 \rangle = \sum_{k=-N/2+1}^{N/2} \langle |s_{jk}|^2 \rangle. \quad (6)$$

Substituting the definition for  $s_{jk}$  and using the fact that  $|A_{j-k} B_k|^2 = |A_{j-k}|^2 |B_k|^2$ , we find

$$\langle |X_j|^2 \rangle = \sum_{k=-N/2+1}^{N/2} \langle |A_{j-k}|^2 \rangle \langle |B_k|^2 \rangle. \quad (7)$$

<sup>3</sup> Note that the complex conjugate symmetry introduced by requiring real time series actually introduces a correlation between  $s_{jk}$  and  $s_{j(-k)}$  terms. However, we show in Appendix A that the resulting pairs of terms behave exactly as if they were uncorrelated.

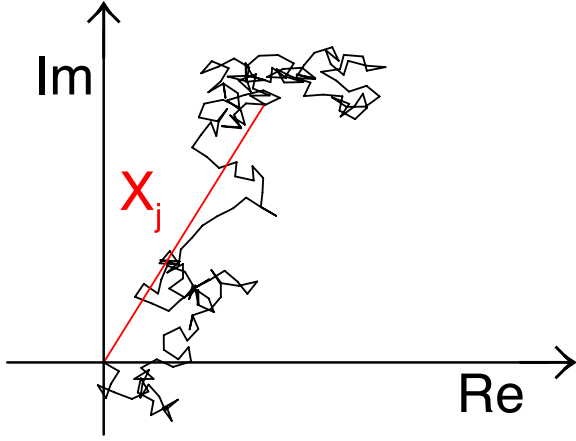


**Figure 1.** Example of a random walk with  $N = 200$  steps each with length  $|s_{jk}| = 1$  in a random direction. The red line represents the complex number  $X_j$  which describes the final position of the walk after  $N$  steps.

Since the averaging here is over infinite realizations, we can write this in terms of power spectra:

$$|X(v_j)|^2 = |A(v_j)|^2 \otimes |B(v_j)|^2, \quad (8)$$

where  $\otimes$  denotes a convolution. We thus have an expression to obtain  $N/2 + 1$  values of the analytic function  $|X(v)|^2$  from  $N/2 + 1$  values of the analytic functions  $|A(v)|^2$  and  $|B(v)|^2$ .

As a demonstration, we compare our analytic calculation to simulations. We take our two input power spectra to be Lorentzians with width  $\Delta v = 20$  and  $10$  Hz and centroid  $v_0 = 10$  and  $60$  Hz, respectively. They are normalized to have a standard deviation in the time domain of  $\sigma = 0.8$  and  $0.4$ , respectively (see van Straaten et al. 2002), and are shown in grey in Fig. 2. We use  $N = 2^{11}$  and  $dt = 2^{-9}$  s and simulate 10 000 time series using the TK95 algorithm before estimating the power spectrum by averaging over all

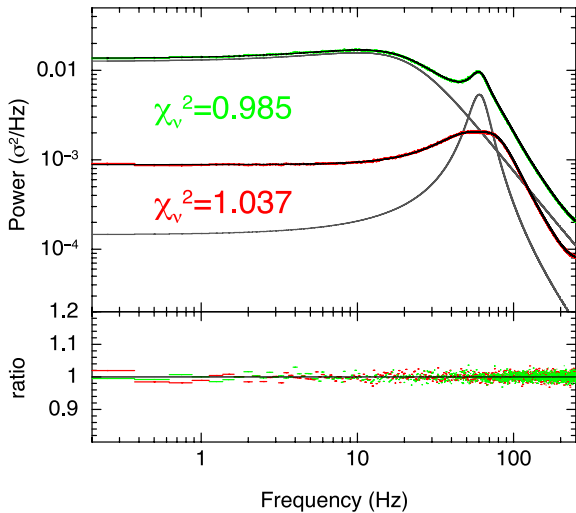


**Figure 2.** Power spectrum of the time series  $x_k = a_k b_k$ , where  $a_k$  and  $b_k$  are stochastic time series with average power spectra given by the grey lines. The red and green points show the power spectrum recovered from simulating  $a_k$  and  $b_k$  with a mean of zero and unity, respectively (the green points are above the red points for readers in black and white). The black lines passing through the simulation results are analytic calculations. The ratio plots (simulation over calculation) and  $\sim$ unity reduced  $\chi^2$  values confirm that the simulation and calculation agree.

realizations (with an error given by the statistical error on the mean, yielding  $1\sigma$  error bars). The red and green points in Fig. 2 show the result of the simulation when the time series have means of  $\mu = 0$  and  $1$ , respectively (the  $\mu = 1$  points are above the  $\mu = 0$  points). The two black lines passing through the simulation points represent the same cases calculated analytically. The ratio plot (simulation divided by calculation) and the  $\chi^2$  confirm that the two methods give the same result for both cases. Note, throughout this paper  $\chi_v^2$  represents reduced  $\chi^2$  (i.e.  $\chi^2/\text{degrees of freedom}$ ).

To understand why changing the input DC components makes such a difference to the final power spectra in Fig. 2, we can re-write equation (8) as

$$|X(v_j)|^2 = |\tilde{A}(v_j)|^2 \otimes |\tilde{B}(v_j)|^2 + \mu_a^2 |\tilde{A}(v_j)|^2 + \mu_b^2 |\tilde{B}(v_j)|^2 + \mu_a^2 \mu_b^2 \delta_{j0}, \quad (9)$$

where  $\delta_{j0}$  is a Kronecker delta and  $\tilde{A}_j = A_j$ ,  $\tilde{B}_j = B_j$  except for  $\tilde{A}_0 = \tilde{B}_0 = 0$ . This shows that changing  $\mu_a$  and  $\mu_b$  to unity for the green line in Fig. 2 has the effect of adding the input functions to the convolution for  $\mu_a = \mu_b = 0$  (i.e. the green line is the sum of the red line and the two grey lines).

### 2.3 Multiplying many time series

The argument of the previous section can be extended to consider  $\mathcal{N}$  time series  $(a_n)_k$  being multiplied together to get  $x_k = \prod_{n=1}^{\mathcal{N}} (a_n)_k$ . Equation (8) can be used  $\mathcal{N} - 1$  times to write the power spectrum of  $x_k$  as

$$|X(v_j)|^2 = \prod_{n=1}^{\mathcal{N}} |A_n(v_j)|^2, \quad (10)$$

where we adopt the co-product symbol to represent a succession of convolutions.

In Fig. 3, we consider an example with  $\mathcal{N} = 30$  functions. The input power spectra are zero-centred Lorentzians with width,  $\Delta v_n$ , changing from  $\Delta v_1 = 5$  Hz to  $\Delta v_{\mathcal{N}} = 40$  Hz and there is an equal

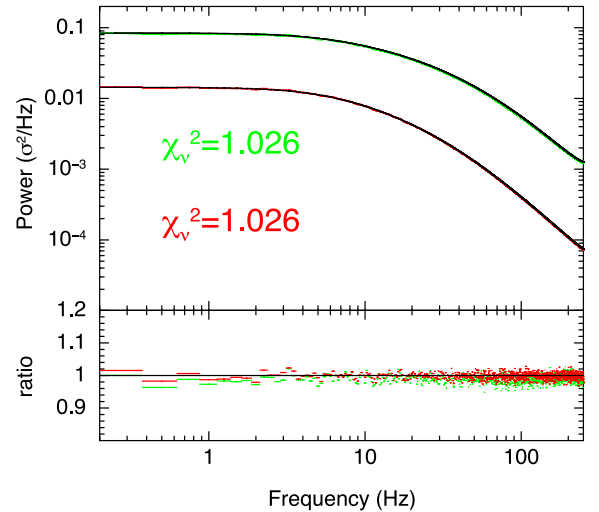


**Figure 3.** The resulting power spectrum when 30 time series are multiplied together (see text for details). The red and green lines represent the simulation results when we give each time series a variance of  $\sigma = 0.5/\sqrt{30}$  and  $1/\sqrt{30}$ , respectively (the green points are above the red points for readers in black and white). The black lines passing through the simulation points are analytic calculations. The ratio plots and  $\sim$ unity reduced  $\chi^2$  values again confirm that the simulation and calculation agree.



logarithmic spacing between the widths of consecutive Lorentzians. All 30 functions have DC components corresponding to a mean  $\mu = 1$  and a standard deviation in the time domain of  $\sigma = \text{rms}/\sqrt{N}$ . For the red and green points, we set  $\text{rms} = 0.5$  and  $1$ , respectively (the  $\text{rms} = 1$  points are above the  $\text{rms} = 0.5$  points). As in Fig. 2, we use  $N = 2^{11}$ ,  $dt = 2^{-9}$  s and average the simulated power spectra over 10 000 realizations. The ratio plots and  $\chi^2$  statistic confirm that the black lines calculated using equation (10) pass identically through the simulation points.

### 3 THE PROPAGATING FLUCTUATIONS MODEL

#### 3.1 Model summary

Here we summarize the propagating fluctuations model of ID12 which we use in this paper with a few small alterations. We consider a flow extending between outer and inner radii  $r_o$  and  $r_i$ , employing the convention that lower case  $r$  is radius expressed in units of  $R_g = GM/c^2$  such that  $r = R/R_g$ . We split the flow into  $N$  rings, each centred at  $r_n$  with an equal logarithmic spacing  $dr_n$  such that  $dr_n/r_n = dr/r = \text{constant}$ . We assume that fluctuations in the local mass accretion rate are stirred up at each ring. These fluctuations are stochastic and therefore have a random phase but they have a well-defined power spectrum given by a zero-centred Lorentzian breaking at the local viscous frequency, i.e.

$$|A_n(\nu)|^2 = \frac{\sigma^2}{T\pi} \frac{\Delta\nu_n}{(\Delta\nu_n)^2 + \nu^2}, \quad (11)$$

where  $\Delta\nu_n = 1/t_{\text{visc}}(r_n)$  and  $\sigma^2$  and  $T$  are the variance and duration of the corresponding time series, respectively. We assume  $\sigma$  is the same for each ring, as is the average,  $\mu$ , which we set to unity. We set  $\sigma/\mu = F_{\text{var}}/\sqrt{N_{\text{dec}}}$ , where  $N_{\text{dec}}$  is the number of rings per radial decade and  $F_{\text{var}}$  is therefore the fractional variability generated per decade.  $F_{\text{var}}$  is thus a physical parameter of the model and  $N_{\text{dec}}$  is a parameter governing the resolution.

This amounts to a physical assumption that each radial decade in the flow generates the same variability power. Simulations often find that the MRI generates noise with this property (e.g. Beckwith, Hawley & Krolik 2008), although we discuss an exception in Section 5. In ID12, we used a slightly different assumption that a constant variability per decade in viscous frequency is generated by the MRI. This helps the model to converge for fewer rings but the physicality of this assumption is questionable. Here, the model is much faster to calculate and so a high required value of  $N$  is no longer prohibitive, thus we revert back to the more physically acceptable assumption adopted in ID11, and also Arévalo & Uttley (2006).

As in ID12, we assume a bending power law form for the time averaged surface density,  $\Sigma(r)$ , which follows  $\Sigma(r) \propto r^{-\zeta}$  for  $r \gg r_{\text{bw}}$  and  $\Sigma(r) \propto r^\lambda$  for  $r \ll r_{\text{bw}}$ . Here  $r_{\text{bw}}$ , the bending wave radius, is the radius at which frame dragging torques set-up plunging streams in the tilted accretion flow simulations of Fragile et al. (2007), Fragile & Meier (2009) and Fragile (2009). This radius is typically larger than the innermost stable circular orbit  $r_{\text{bw}} \sim 4\text{--}11$  (see Ingram et al. 2009). Long-term mass conservation then yields an expression for the local viscous time-scale,  $t_{\text{visc}}(r_n) = 2\pi R_n^2 \Sigma(r_n)/\dot{m}_0$ , where  $\dot{m}_0$  is the time averaged mass accretion rate. Thus, the viscous time-scale also has a bending power law form.

The fluctuations generated in every ring will propagate inwards such that the local mass accretion rate at  $r_n$  is given by

$$\dot{m}(r_n, t) = \dot{m}_0 \prod_{l=1}^n a_l(t - \Delta t_{ln}), \quad (12)$$

where  $\Delta t_{ln}$  is the propagation time from  $r_l$  to  $r_n$ , given by

$$\Delta t_{ln} = \frac{dr}{r} \sum_{q=l+1}^n t_{\text{visc}}(r_q). \quad (13)$$

Thus, for example  $\Delta t_{nn} = 0$  and  $\Delta t_{(n-1)n} = dr/r t_{\text{visc}}(r_n)$ . This can be alternatively written in terms of the mass accretion rate in the  $(n-1)$ th ring:

$$\dot{m}(r_n, t) = a_n(t) \dot{m}(r_{n-1}, t - \Delta t_{(n-1)n}). \quad (14)$$

Thus, at the outermost ring,  $r_1$ , the locally generated fluctuations will only be multiplied by the average mass accretion rate  $\dot{m}_0$  whereas rings closer to the black hole will be modulated with fluctuations generated at all outer rings.

The *total* (over all energies) luminosity available to be radiated in the  $n$ th ring is  $\propto \dot{m}(r_n, t)$ . If the energy dependence of emission from each ring stays constant in time, then the flux observed in some energy band can be written as

$$f_h(t) = \sum_{n=1}^N h_n \dot{m}(r_n, t), \quad (15)$$

where  $h_n$  is a set of weighting factors and we apply the convention that  $f_h(t)$  is the hard band flux (since we fit the model to the  $>10$  keV power spectrum in ID11 and ID12). The ID12 model assumes  $h_n \propto dr/r r_n^{2-\gamma_h} b(r_n)$ , with the boundary condition  $b(r_n) \propto \Sigma(r_n)$ . In a truncated disc geometry, we expect the inner, more photon starved regions of the flow to emit a harder spectrum than the cooler outer regions implying a steeper emissivity for higher energy bands; i.e.  $\gamma_s < \gamma_h$ , where ‘s’ denotes a soft band. It is this physical property that allows the propagating fluctuations model to predict the observed lag between hard and soft energy bands (Kotov et al. 2001; Arévalo & Uttley 2006).

#### 3.2 Power spectrum of the local mass accretion rate

We can use the result from Section 2 along with the ‘time shifting’ property of Fourier transforms in order to find that the power spectrum of the mass accretion rate at  $r_n$  is given by

$$|\dot{M}(r_n, \nu)|^2 = |A_n(\nu)|^2 \otimes |e^{i2\pi\Delta t_{(n-1)n}\nu} \dot{M}(r_{n-1}, \nu)|^2. \quad (16)$$

Note here and for the rest of the paper we represent power spectra (and also time series and their Fourier transforms) as continuous rather than explicitly evaluating all power spectra at discrete frequencies  $\nu_j$ . The phase shift clearly cancels here and so we can write the power spectrum of the mass accretion rate at  $r_n$  as

$$|\dot{M}(r_n, \nu)|^2 = \dot{m}_0^2 \prod_{l=1}^n |A_l(\nu)|^2. \quad (17)$$

We compute the convolutions by transforming into the time domain using fast Fourier transforms (FFTs), multiplying and then transforming back with FFTs. This is by far the most computationally efficient method to compute a convolution (Press et al. 1992).

#### 3.3 Power spectrum for a given energy band

We now calculate the power spectrum of the ‘hard band’ flux  $f_h(t)$  (note this is a nominal choice, we have simply defined the radial

emissivity as a power law). We can transform equation (15) and take the modulus squared to show

$$P(\nu) = |F_h(\nu)|^2 = \sum_{l,n=1}^{\mathcal{N}} h_l h_n \dot{M}(r_l, \nu)^* \dot{M}(r_n, \nu), \quad (18)$$

where  $l$  and  $n$  both take every value between 1 and  $\mathcal{N}$ . The terms with  $l = n$  are easy to evaluate since they reduce to  $h_n^2 |\dot{M}(r_n, \nu)|^2$ . To evaluate the other terms (the cross-spectra), we must appreciate which components of the mass accretion rate from different rings are coherent. We show in Appendix B that the cross-spectra are given by

$$\dot{M}(r_l, \nu)^* \dot{M}(r_n, \nu) = \dot{m}_0 \Lambda_{ln} e^{i2\pi \Delta t_{ln} \nu} |\dot{M}(r_l, \nu)|^2, \quad (19)$$

where  $n > l$  and  $\Lambda_{ln} \equiv \prod_{q=l+1}^n \mu_q$ . For this model, we always set  $\mu = 1$  so this product reduces to unity. However, to preserve generality, we leave it in the resulting equation for the power:

$$P(\nu) = \sum_{n=1}^{\mathcal{N}} \left[ h_n^2 |\dot{M}(r_n, \nu)|^2 + 2 \sum_{l=1}^{n-1} h_l h_n \Lambda_{ln} \cos(2\pi \Delta t_{ln} \nu) |\dot{M}(r_l, \nu)|^2 \right], \quad (20)$$

where we have used the fact that the conjugate of  $\dot{M}(r_l, \nu)^* \dot{M}(r_n, \nu)$  is  $\dot{M}(r_n, \nu)^* \dot{M}(r_l, \nu)$ . Thus we have a simple sum plus cross terms which represent interference between contributions from each ring. The phase lag between radiation from different rings determines whether the interference is constructive or destructive. We see that all the cross terms will cancel if we set all  $\mu_n = 0$ . This makes sense physically because, in this case, the mean local mass accretion rate inside  $r_0$  is zero and thus no fluctuations can propagate leaving radiation emitted from different rings uncorrelated.

In Fig. 4, we plot the power spectrum predicted by the model using both simulation and equation (20). We use the best-fitting

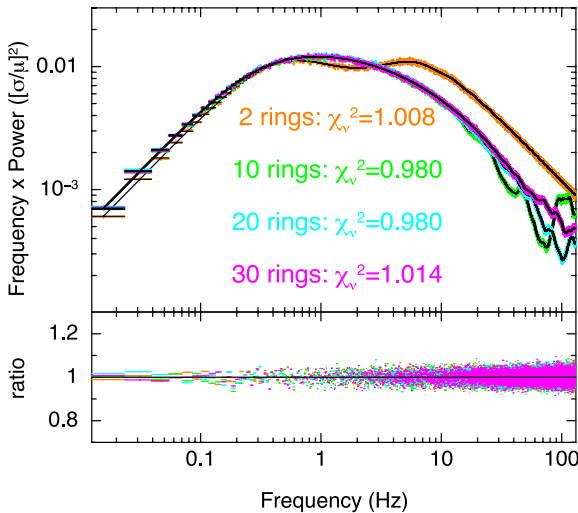


**Figure 4.** Power spectrum, normalized to show fractional variability, predicted from the model parameters in the text. Different colours represent different model resolution with  $N_{\text{dec}} = 3, 12, 23, 35$  corresponding to 2, 10, 20 and 30 rings, respectively (for readers in black and white, the lowest resolution model shows two distinct bumps and after that higher resolutions display less oscillatory behaviour at high frequency). The points with error represent a simulation averaged over 2000 iterations, whereas the black lines are calculated from equation (20). The ratio plots and reduced  $\chi^2$  values confirm that the simulation reproduces the analytical result.

parameters found for observation 3 in ID12 (except here we do not include the QPO). We thus set  $r_0 = 25$ ,  $r_i = 3.3$ ,  $r_{\text{bw}} = 8.7$ ,  $\lambda = 0.9$ ,  $\zeta = 0$ ,  $\gamma_h = 5.3$  and  $F_{\text{var}} = 0.3$ . We assume a black hole mass and spin of  $M = 10 M_\odot$  and  $a_* = 0.5$ , respectively, throughout this paper. The simulated power spectra are plotted with  $(1\sigma)$  errors and the black lines show the analytically calculated power spectra. We vary the resolution of the model showing four examples with orange, green, cyan and magenta representing  $N_{\text{dec}} = 3, 12, 23$  and  $35$ , respectively (for readers in black and white, see the figure caption). These values are chosen to give 2, 10, 20 and 30 rings in total. The ratio plots and  $\chi^2$  values confirm that the predicted power spectrum for a given set of model parameters is identical whether we simulate or use equation (20). We also see the effect of interference (the cosine term in equation 20) on the power spectral shape for different numbers of rings.

### 3.4 Cross-spectrum for two given energy bands

In the previous section, we calculated the power spectrum of our nominal hard band. It is clear that the power spectrum of some other (soft) band can also be calculated from equation (20) by using a different emissivity (i.e. substituting ‘s’ for ‘h’). We can go one step further and calculate the time lags between the two bands. These can be found using the cross-spectrum,  $C(\nu) = F_h(\nu)^* F_s(\nu)$  which, in contrast to the power spectrum, is complex. The phase lag between radiation from the two bands is given by  $\tan[\Phi(\nu)] = \Im[C(\nu)]/\Re[C(\nu)]$  and the corresponding time lag is simply  $t_{\text{lag}}(\nu) = \Phi(\nu)/(2\pi\nu)$ .

It is relatively simple to adapt equation (20) to show that the cross-spectrum is given by

$$C(\nu) = \sum_{n=1}^{\mathcal{N}} \left[ h_n s_n |\dot{M}(r_n, \nu)|^2 + \sum_{l=1}^{n-1} (h_l s_n e^{i2\pi \Delta t_{ln} \nu} + h_n s_l e^{-i2\pi \Delta t_{ln} \nu}) \Lambda_{ln} |\dot{M}(r_l, \nu)|^2 \right]. \quad (21)$$

This can be separated out into real and imaginary parts by splitting the exponentials into sines and cosines to give

$$\Re[C(\nu)] = \sum_{n=1}^{\mathcal{N}} \left[ h_n s_n |\dot{M}(r_n, \nu)|^2 + \sum_{l=1}^{n-1} (h_l s_n + h_n s_l) \cos(2\pi \Delta t_{ln} \nu) \Lambda_{ln} |\dot{M}(r_l, \nu)|^2 \right] \quad (22)$$

for the real part and

$$\Im[C(\nu)] = \sum_{n=1}^{\mathcal{N}} \sum_{l=1}^{n-1} (h_l s_n - h_n s_l) \sin(2\pi \Delta t_{ln} \nu) \Lambda_{ln} |\dot{M}(r_l, \nu)|^2 \quad (23)$$

for the imaginary part.

In Fig. 5, we plot the predicted time lags using the same model parameters as in the previous section with the additional assumption that the soft band emissivity index is  $\gamma_s = 4.5$ . Again, orange, green, cyan and magenta represent 2, 10, 20 and 30 rings, respectively (for readers in black and white, see the figure caption) and the points with error bars are from simulation whereas the lines are calculated analytically (equations 22 and 23). We calculate the errors on the simulation using the formula from Nowak et al. (1999). Again, the  $\chi^2$  values confirm the simulation returns the same result as the

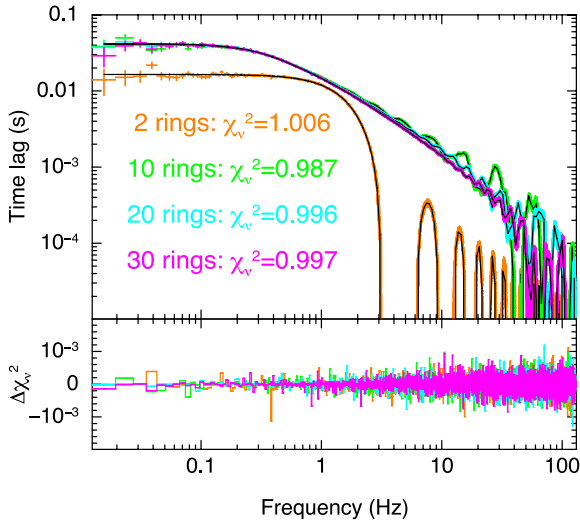


**Figure 5.** Lag spectrum predicted using the model parameters in the text. As in Fig. 4, different colours represent  $N_{\text{dec}} = 3, 12, 23$  and  $35$ , corresponding to 2, 10, 20 and 30 rings, respectively (for readers in black and white, lower resolution models are associated with increasingly oscillatory behaviour). Again, the points with error represent the simulation and the black lines are calculated analytically, with the two showing excellent agreement (quantified by the  $\sim$ unity reduced  $\chi^2$  values). Here, we averaged the simulation over 2000 realizations.

analytical expression. We plot contributions to  $\chi_v^2$  (positive means the simulation points are above the calculation) instead of ratio because the lag spectrum passes through zero for some parameter values. We see that at least 30 rings are required to achieve convergence. In fact, even the 30 ring model is slightly under-resolved with oscillatory behaviour above  $\nu \approx 10$  Hz. However, this occurs well below the Poisson noise level for currently available observational data. This will not be the case for the Large Area Detector (LAD), the primary instrument of the proposed European Space Agency mission the *Large Observatory For X-ray Timing* (LOFT; Feroci et al. 2012), which will have a collecting area  $\sim 20$  times that of *RXTE*.

### 3.5 Including the QPO

Ingram et al. (2009) proposed that the QPO (i.e. the type C QPO, including all harmonics), is due to Lense–Thirring precession of the entire flow. The model of ID12 calculates the precession frequency,  $\nu_{\text{prec}}$ , from the surface density profile and the inner and outer flow radii. The power spectrum of the QPO is then taken as a sum of Lorentzians peaking at  $\nu_{\text{prec}}$ ,  $2\nu_{\text{prec}}$ ,  $3\nu_{\text{prec}}$  and  $\nu_{\text{prec}}/2$  representing the fundamental, second, third and subharmonics, respectively, with the width of the fundamental  $\Delta\nu_{\text{qpo}}$  left as a free parameter. The width of the second and third harmonics are then fixed at  $2\Delta\nu_{\text{qpo}}$  and  $3\Delta\nu_{\text{qpo}}$ , respectively, with the width of the subharmonic left free (since the subharmonic is often observed to have a different width; Rao et al. 2010). ID12 generate a light curve from this using the TK95 algorithm and add this to the light curve generated from the propagating fluctuations simulation. For simplicity, the final light curve is normalized such that its power spectrum is equal to the sum of the two component power spectra. This is not particularly realistic since this normalization implies that at least one of the two component light curves has zero mean. However, it provides the simplest possible way of fixing model parameters using both the QPO frequency and the shape of the broad-band noise.

For a more realistic treatment, we must consider the physical mechanism by which the precession frequency modulates the emission. The two most significant modulation mechanisms will be *projected area variation* as the brightest patch of the flow moves in and out of the observer’s line of sight (see Ingram & Done 2012b) and also *seed photon variation* as the flux of disc photons incident on the flow changes as a function of precession phase. In this paper, we consider both an additive (appropriate for seed photon variation) and a multiplicative model (appropriate for projected area variation). For the additive model, we use exactly the same treatment as in ID12: the overall flux is  $f_{\text{tot}}(t) = f(t) + Q(t)$ , where  $Q(t)$  and  $f(t)$  contain, respectively, the quasi-periodic and aperiodic variability. Here,  $f(t)$  has a mean of unity, whereas  $Q(t)$  has a mean of zero. Since we have assumed the two processes to be uncorrelated, the final power spectrum will be the sum of the powers for each process. For the multiplicative model, we take the overall flux to be  $f_{\text{tot}}(t) = f(t)Q(t)$ , where  $Q(t)$  now has a mean of unity. The assumption that these two processes are uncorrelated now leads to the final power spectrum being a convolution between the powers of each process. Note that, in principle, we could also investigate other QPO mechanisms in this manner. For example, we could replace one of the  $\dot{m}(r_n, t)$  functions with a quasi-periodic function  $Q(t)$  to represent some oscillating mode in a narrow region of the accretion flow.

## 4 EXAMPLE FITS TO RXTE DATA

Here we fit the model to *RXTE* data from the 1998 outburst of the transient BHB XTE J1550–564. We look at one observation from the intermediate state of this outburst with observational ID 30188-06-01-03, referred to in ID12 as observation 3. We calculate the white noise subtracted power spectrum of the 13.36–27 keV light curve by averaging over 15 intervals, each containing  $2^{15}$  time bins of length  $\Delta t = 2^{-8}$  s, and re-bin geometrically using a re-binning constant of 1.05 (van der Klis 1989). We further group bins in which the power is averaged over less than 200 raw periodogram points. This ensures that the statistical error on the mean periodogram has converged to the Gaussian limit for each bin and thus the use of  $\chi^2$  as a fit statistic is appropriate.

We first fit the additive model, which treats the QPO in the same way as ID12, setting  $N_{\text{dec}} = 30$ . We use XSPEC version 12 (Arnaud, Borkowski & Harrington 1996) to find the best least-squares fit, freezing all the parameters that were held constant in ID12. Fig. 6 (top) shows the result plotted in frequency  $\times$  power with the contributions to  $\chi^2$  also plotted underneath. The best-fitting parameters, shown in Table 1, give a minimum  $\chi_v^2 = 107.31/88 = 1.22$ . We also fit the multiplicative model for which the QPO power spectrum is convolved with that of the broad-band noise instead of added. We find the fit plotted in Fig. 6 (bottom) is slightly better ( $\chi_v^2 = 106.46/88 = 1.21$ ), although the difference is not significant. The main difference between the two sets of parameters is  $F_{\text{var}}$  which is smaller for the multiplicative model because here the final power spectrum is a sum of the broad-band noise, the QPO and the convolution between the AC components of these two components (see equation 9) which enhances the total variability predicted for a given value of  $F_{\text{var}}$ .

We simulate both versions of the model with 1000 realizations to confirm convergence to the analytic calculation. For the additive and multiplicative models we find agreement between simulated and calculated power with  $\chi_v^2 = 1.0164$  and  $1.014$ , respectively (both for  $2^{15}$  degrees of freedom). We also simulate using only 15 realizations to directly compare the simulation to data. When we

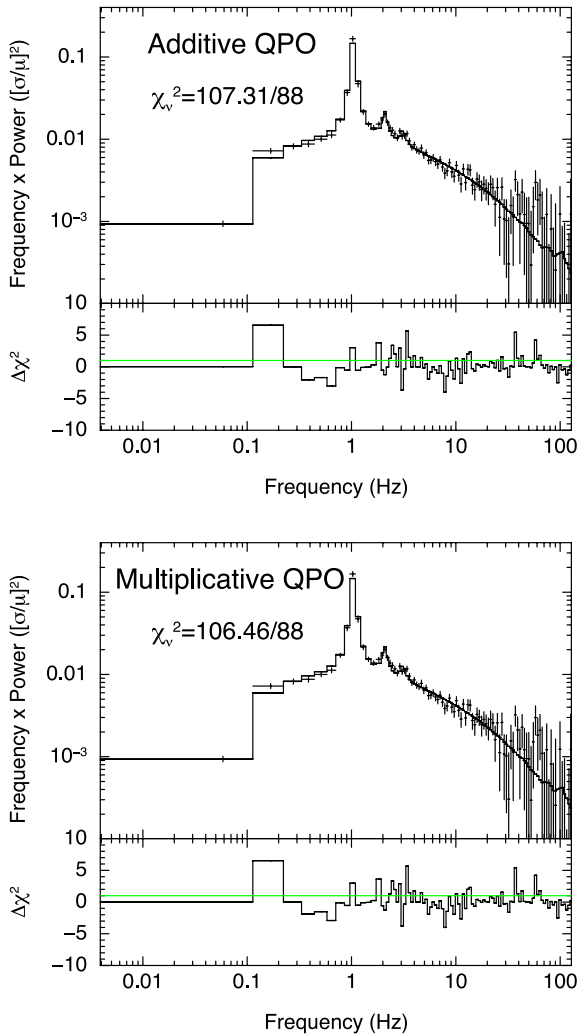


**Figure 6.** White noise subtracted 13.36–27 keV power spectrum of observational ID 30188-06-01-03 with best-fitting additive (top) and multiplicative (bottom) models (see Table 1).

**Table 1.** Best-fitting parameters with associated ( $1\sigma$ ) error estimates for the additive and multiplicative models (see Fig. 6) alongside those from ID12.

Parameter	Additive QPO	Multiplicative QPO	ID12
$\Sigma_0$ ( $\dot{M}_0/[cR_g]$ )	$27.34 \pm 3.37$	$28.09 \pm 2.86$	$23.67 \pm 4.45$
$r_{\text{bw}}$ ( $R_g$ )	$10.86 \pm 1.60$	$11.21 \pm 1.80$	$6.80 \pm 1.10$
$\kappa$	$\equiv 3$	$\equiv 3$	$\equiv 3$
$\lambda$	$\equiv 0.9$	$\equiv 0.9$	$\equiv 0.9$
$\zeta$	$\equiv 0$	$\equiv 0$	$\equiv 0$
$F_{\text{var}}$	$0.276 \pm 0.01$	$0.138 \pm 0.008$	$0.372 \pm 0.018$
$r_o$ ( $R_g$ )	$24.422 \pm 0.48$	$24.32 \pm 0.10$	$26.03 \pm 0.49$
$r_i$ ( $R_g$ )	$\equiv 3.3$	$\equiv 3.3$	$\equiv 3.3$
$\Delta\nu_{\text{QPO}}$ ( $10^{-2}$ Hz)	$7.05 \pm 0.46$	$7.03 \pm 0.46$	$6.12 \pm 0.47$
$\sigma_{\text{qpo}}$ ( $10^{-2}$ )	$17.16 \pm 0.46$	$17.13 \pm 0.47$	$17.18 \pm 0.47$
$\sigma_{2\text{qpo}}$ ( $10^{-2}$ )	$4.94 \pm 0.27$	$4.93 \pm 0.27$	$4.80 \pm 0.25$
$\sigma_{3\text{qpo}}$ ( $10^{-2}$ )	$2.94 \pm 0.26$	$2.93 \pm 0.28$	$2.78 \pm 0.26$
$\gamma$	$5.39 \pm 0.27$	$5.56 \pm 0.37$	$4.97 \pm 0.53$
$M$ ( $M_\odot$ )	$\equiv 10$	$\equiv 10$	$\equiv 10$
$a$	$\equiv 0.5$	$\equiv 0.5$	$\equiv 0.5$
$\chi^2_v$	107.31/88	106.46/88	120.96/88

use the binning scheme described above, we find that the simulation does converge to the analytic calculation with reduced  $\chi^2$  values of 1.004 and 1.014, respectively, for the additive and multiplicative versions of the model (both for 97 degrees of freedom). Thus, if our model did perfectly describe the observed data, it would indeed return a reduced  $\chi^2$  of unity. Table 1 also shows the result of re-fitting the ID12 model using the analytic formulation. The new best-fitting parameters are close to those obtained in ID12 using the simulation method (with the fitting algorithm taking minutes to run for the analytical calculation as opposed to weeks for the old simulation method) and give a reduced  $\chi^2$  value of  $\chi^2_v = 120.96/88 = 1.37$ .

It is possible to see from Fig. 6 that both models predict the slope between  $\sim 0.1$  and 1 Hz to be too steep (this can also be seen in the contributions to  $\chi^2$ ). In the hard state of most BHBs when there is no (or only a weak) QPO present, it is possible to see by eye that the broad-band noise is best modelled by two (or perhaps more) discrete bumps rather than the ‘flat top’ noise predicted by this model. It is possible that the broad-band noise in this intermediate state power spectrum is also best modelled with two discrete bumps, resulting in the small discrepancy between our model and the data. We will discuss the potential physical implications of this in the following section.

Although the power spectra for the additive and multiplicative models are only subtly different, the predicted bi-coherence (Maccarone & Coppi 2002) will be extremely different. This is a measure of correlation between different Fourier frequencies and reveals that the QPO correlates strongly with the broad-band noise in GRS 1915+105 (Maccarone et al. 2011) and also for the observation of XTE J1550–564 considered here (Maccarone, private communication). This strong correlation cannot be reproduced by the additive model but potentially could by the multiplicative model, strongly favouring the latter.

## 5 DISCUSSION AND CONCLUSIONS

The model of ID11 and ID12 combines propagating mass accretion rate fluctuations with Lense–Thirring precession of the inner flow to fit a physical model to a BHB power spectrum for the first time. In these papers, and previous studies of the propagating fluctuations model (Arévalo & Uttley 2006), a Monte Carlo simulation is used to generate stochastic light curves and the power spectrum is *estimated* by averaging over many realizations. This process is heavily computationally intensive and inevitably leads to an inexact model with an associated error estimate. Here, we calculate the *same* model *exactly* by deriving an analytic formula. We find that, in this context, the power of mass accretion rate fluctuations from a given region of the flow at each Fourier frequency is a random walk on the complex plane and a standard statistical result gives an exact expression. We then derive an exact expression for the power spectrum of *any* linear combination of these mass accretion rate functions. We can thus calculate the ID12 model exactly. We fit our model to an observation previously considered in ID12. We can now, in contrast to ID12, fully explore  $\chi^2$  space and run error calculations. We obtain a fairly good fit with residuals which hint at changes we must make to our physical assumptions going forward. We also find that the more physical assumption of a multiplicative QPO gives a marginally better fit than the previously assumed additive QPO.

The model here still ignores intrinsic disc variability. Since this has been observationally confirmed in the hard state (Wilkinson & Uttley 2009), it will be more appropriate to consider noise to be generated in both the disc and flow with a discontinuity in viscous



time-scale occurring at the truncation radius (since this will be shorter in the flow than in the disc). This discontinuity in viscous time-scale will allow the model to reproduce the double hump power spectra often observed in the hard state and may even improve the fit for intermediate state power spectra such as the observation considered here. The model also assumes that the MRI generates equal variability power per decade in radius. In ID12, we speculated that frame dragging torques could give rise to enhanced variability in the bending wave region. We showed that, for this effect to give rise to a bumpy power spectrum, the variability in the bending wave region needs to be a factor of  $\sim 10$  greater than elsewhere (fig. 6 therein). Henisey, Blaes & Fragile (2012) have since found that the tilted accretion flow GRMHD simulations of Fragile et al. (2007) do indeed show enhanced variability in the bending wave region (see fig. 7 therein) a factor of  $\sim 10$  greater than elsewhere! Thus we may need to consider this going forward.

There are a number of other obvious improvements we can make to the model. We stress that our result here is *very* powerful since it can still be used with far more sophisticated versions of the model than the one considered here. First of all, the ID12 model effectively assumes an overly simplified form for the power spectrum of the Green's function (the Green's power) of the flow. The true Green's function for a Keplerian flow can be found from the diffusion equation (Lynden-Bell & Pringle 1974; Pringle 1981; Frank et al. 2002; King et al. 2004) and, providing the system is linear, can be convolved with any intrinsic fluctuations generated by, say, the MRI to give the resulting fluctuations in mass accretion rate. In Fourier space, this is a multiplication and thus if the input fluctuations are white noise, the power spectrum of the mass accretion rate simply becomes the Green's power. In general, the Green's power is a function  $G(r_l, r_n, \nu)$ , where  $r_l$  and  $r_n$  are, respectively, the radii at which the fluctuation was generated and reacted to. In the limit  $r_l \gg r_n$ , the Green's power becomes a zero-centred Lorentzian with width  $1/t_{\text{visc}}(r_n)$  (equation 11). Since the analytic formulae we derive here are appropriate for *any* Green's function, we will apply it in future to a more general Green's function derived directly from the diffusion equation.

Also, we have thus far assumed that the Compton upscattering process which creates the power-law emission is effectively instantaneous. In reality, this process will also contribute a Green's function with a power spectrum that looks like a low-pass filter with a break at fairly high frequency. Ishibashi & Courvoisier (2012) speculate that the high-frequency break in the observed power spectrum could be associated with the Compton cooling time-scale in the flow. If this time-scale dictates the break frequency in the Compton Green's power, it will indeed govern the observed high-frequency break in the power spectrum. Since this time-scale naturally predicts McHardy et al.'s (2006) empirical relation with mass and accretion rate, it is a very attractive suggestion. We will investigate this in a future paper. Also, we assume that the flux in a given energy band is a linear combination of the mass accretion rate at each radius. In reality, this will not be completely true since the spectral *shape* of emission from each ring will vary with mass accretion rate. Gierliński & Zdziarski (2005) studied the effect of varying certain parameters of a Comptonization model. We plan to include a similar analysis in a future version of our model.

In conclusion, we have shown that the power spectral model of ID12 can be calculated analytically. We have also shown simple ways of calculating the predicted power spectrum for different energy bands and even the time lag between energy bands. Going forward, we can thus fit simultaneously to all of these observational

properties, utilizing the wealth of information locked in the spectral timing properties of the X-ray data.

## ACKNOWLEDGEMENTS

We acknowledge the anonymous referee for very useful comments facilitating the clarity and swift completion of this work. This research has made use of data obtained through the High Energy Astrophysics Science Archive Research Center Online Service, provided by the NASA/Goddard Space Flight Center.

## REFERENCES

- Altamirano D., Ingram A., van der Klis M., Wijnands R., Linares M., Homan J., 2012, *ApJ*, 759, L20
- Arévalo P., Uttley P., 2006, *MNRAS*, 367, 801
- Arnaud K., Borkowski K. J., Harrington J. P., 1996, *ApJ*, 462, L75
- Balbus S. A., Hawley J. F., 1998, *Rev. Modern Phys.*, 70, 1
- Beckwith K., Hawley J. F., Krolik J. H., 2008, *MNRAS*, 390, 21
- Belloni T. M., 2010, in Comastri A., Angelini L., Cappi M., eds, *AIP Conf. Ser. Vol. 1248, X-Ray Astronomy 2009: Present Status, Multi-Wavelength Approach and Future Perspectives*. Am. Inst. Phys., New York, p. 107
- Belloni T., Psaltis D., van der Klis M., 2002, *ApJ*, 572, 392
- Cabanac C., Henri G., Petrucci P.-O., Malzac J., Ferreira J., Belloni T. M., 2010, *MNRAS*, 404, 738
- Churazov E., Gilfanov M., Revnivtsev M., 2001, *MNRAS*, 321, 759
- Davies R. B., Harte D. S., 1987, *Biometrika*, 74, 96
- Done C., Gierliński M., Kubota A., 2007, *A&AR*, 15, 1
- Esin A. A., McClintock J. E., Narayan R., 1997, *ApJ*, 489, 865
- Feroci M. et al., 2012, *Proc. SPIE*, 8443, 84432D
- Fragile P. C., 2009, *ApJ*, 706, L246
- Fragile P. C., Meier D. L., 2009, *ApJ*, 693, 771
- Fragile P. C., Mathews G. J., Wilson J. R., 2001, *ApJ*, 553, 955
- Fragile P. C., Blaes O. M., Anninos P., Salmonson J. D., 2007, *ApJ*, 668, 417
- Frank J., King A., Raine D. J., 2002, *Accretion Power in Astrophysics*, 3rd edn. Cambridge Univ. Press, Cambridge
- Gierliński M., Zdziarski A. A., 2005, *MNRAS*, 363, 1349
- Gilfanov M., 2010, in Belloni T., ed., *Lecture Notes in Physics*, Vol. 794, The Jet Paradigm. Springer-Verlag, Berlin, p. 17
- Gilfanov M., Churazov E., Revnivtsev M., 2000, *MNRAS*, 316, 923
- Hawley J. F., Balbus S. A., 1991, *ApJ*, 376, 223
- Heil L. M., Vaughan S., Uttley P., 2011, *MNRAS*, 411, L66
- Heil L. M., Vaughan S., Uttley P., 2012, *MNRAS*, 422, 2620
- Henisey K. B., Blaes O. M., Fragile P. C., 2012, *ApJ*, 761, 18
- Homan J., Wijnands R., van der Klis M., Belloni T., van Paradijs J., Klein-Wolt M., Fender R., Méndez M., 2001, *ApJS*, 132, 377
- Ichimaru S., 1977, *ApJ*, 214, 840
- Ingram A., Done C., 2010, *MNRAS*, 405, 2447
- Ingram A., Done C., 2011, *MNRAS*, 415, 2323 (ID11)
- Ingram A., Done C., 2012a, *MNRAS*, 419, 2369 (ID12)
- Ingram A., Done C., 2012b, *MNRAS*, 427, 934
- Ingram A., Done C., Fragile P. C., 2009, *MNRAS*, 397, L101
- Ishibashi W., Courvoisier T. J.-L., 2012, *A&A*, 540, L2
- King A. R., Pringle J. E., West R. G., Livio M., 2004, *MNRAS*, 348, 111
- Klein-Wolt M., van der Klis M., 2008, *ApJ*, 675, 1407
- Kotov O., Churazov E., Gilfanov M., 2001, *MNRAS*, 327, 799
- Lynden-Bell D., Pringle J. E., 1974, *MNRAS*, 168, 603
- Lyubarskii Y. E., 1997, *MNRAS*, 292, 679
- Maccarone T. J., Coppi P. S., 2002, *MNRAS*, 336, 817
- Maccarone T. J., Uttley P., van der Klis M., Wijnands R. A. D., Coppi P. S., 2011, *MNRAS*, 413, 1819
- McHardy I. M., Koerding E., Knigge C., Uttley P., Fender R. P., 2006, *Nat*, 444, 730
- Marković D., Lamb F. K., 1998, *ApJ*, 507, 316

- Miyamoto S., Kitamoto S., 1989, *Nat*, 342, 773
- Novikov I. D., Thorne K. S., 1973, in DeWitt C., DeWitt B. S., eds, *Black Holes*. Gordon & Breach, New York, p. 343
- Nowak M. A., Vaughan B. A., Wilms J., Dove J. B., Begelman M. C., 1999, *ApJ*, 510, 874
- Oppenheim A. V., Schaffer R. W., 1975, *Digital Signal Processing*. Prentice-Hall, Englewood Cliffs, NJ
- Press W. H., Teukolsky S. A., Vetterling W. T., Flannery B. P., 1992, *Numerical Recipes in Fortran*, 2nd edn. Cambridge Univ. Press, Cambridge
- Pringle J. E., 1981, *ARA&A*, 19, 137
- Rao F., Belloni T., Stella L., Zhang S. N., Li T., 2010, *ApJ*, 714, 1065
- Schnittman J. D., 2005, *ApJ*, 621, 940
- Schnittman J. D., Homan J., Miller J. M., 2006, *ApJ*, 642, 420
- Shakura N. I., Sunyaev R. A., 1973, *A&A*, 24, 337
- Skipper C. J., McHardy I. M., Maccarone T. J., 2013, *MNRAS*, preprint (arXiv:1306.2475)
- Sobolewska M. A., Życki P. T., 2006, *MNRAS*, 370, 405
- Sobolewska M. A., Papadakis I. E., Done C., Malzac J., 2011, *MNRAS*, 417, 280
- Stella L., Vietri M., 1998, *ApJ*, 492, L59
- Sunyaev R. A., Truemper J., 1979, *Nat*, 279, 506
- Tagger M., Pellat R., 1999, *A&A*, 349, 1003
- Terrell N. J., Jr, 1972, *ApJ*, 174, L35
- Thorne K. S., Price R. H., 1975, *ApJ*, 195, L101
- Timmer J., Koenig M., 1995, *A&A*, 300, 707 (TK95)
- Titarchuk L., Osherovich V., 1999, *ApJ*, 518, L95
- Uttley P., McHardy I. M., 2001, *MNRAS*, 323, L26
- Uttley P., McHardy I. M., Vaughan S., 2005, *MNRAS*, 359, 345
- Uttley P., Wilkinson T., Cassatella P., Wilms J., Pottschmidt K., Hanke M., Böck M., 2011, *MNRAS*, 414, L60
- van der Klis M., 1989, *ARA&A*, 27, 517
- van der Klis M., 2006, in Lewin W., van der Klis M., eds, *Compact Stellar X-Ray Sources*. Cambridge Univ. Press, Cambridge, p. 39
- van Straaten S., van der Klis M., di Salvo T., Belloni T., 2002, *ApJ*, 568, 912
- Vaughan B. A., Nowak M. A., 1997, *ApJ*, 474, L43
- Wagoner R. V., Silbergleit A. S., Ortega-Rodríguez M., 2001, *ApJ*, 559, L25
- Weiss G. H., 1994, *Aspects and Applications of the Random Walk*. North-Holland, Amsterdam
- Weisskopf M. C., Kahn S. M., Sutherland P. G., 1975, *ApJ*, 199, L147
- Wijnands R., van der Klis M., 1999, *ApJ*, 514, 939
- Wilkinson T., Uttley P., 2009, *MNRAS*, 397, 666

## APPENDIX A: COMPLEX CONJUGATE SYMMETRY

The derivation of equation (8) relies on the assumption that the two time series being multiplied together,  $a_k$  and  $b_k$ , are completely uncorrelated. That this is indeed the case is not as trivial as it first seems since the fact that  $a_k$  and  $b_k$  are real introduces a correlation between  $A_j$  and  $A_{-j}$  (complex conjugate symmetry). To illustrate this point, consider  $a_k$  and  $b_k$  with only  $N = 4$  terms. Using equation (5), we know that the  $j = 2$  entry of the DFT of  $x_k = a_k b_k$  obeys

$$\sqrt{4\pi} X_2 = |A_{-1}||B_{-1}|e^{i(\alpha_{-1}+\beta_{-1})} + |A_2||B_0|e^{i(\alpha_2+\beta_0)} \\ + |A_1||B_1|e^{i(\alpha_1+\beta_1)} + |A_0||B_2|e^{i(\alpha_0+\beta_2)}. \quad (\text{A1})$$

Here  $\alpha_j$  and  $\beta_j$  represent the phase of  $A_j$  and  $B_j$ , respectively. Since  $\alpha_{-j} = -\alpha_j$  and  $\beta_{-j} = -\beta_j$ , we see that the  $A_{-1}B_{-1}$  and  $A_1B_1$  terms are correlated with each other such that

$$A_{-1}B_{-1} + A_1B_1 = 2|A_1||B_1|\cos(\alpha_1 + \beta_1). \quad (\text{A2})$$

Thus, these two terms actually behave in the sum (equation A1) as one larger term. When we then calculate  $|X_2|^2$ , the sum will contain one term of size  $4|A_1|^2|B_1|^2\cos^2(\alpha_1 + \beta_1)$  rather than two terms with combined size  $2|A_1|^2|B_1|^2$ . However, when we calculate  $\langle |X_2|^2 \rangle$ , we find  $\langle \cos^2(\alpha_1 + \beta_1) \rangle = 1/2$  and therefore this one large term contributes  $2|A_1|^2|B_1|^2$ ; the same as the total contribution of two uncorrelated terms. For general  $N$ ,  $A_{-j}B_{-j}$  correlates with  $A_jB_j$  and  $A_{-j}B_j$  correlates with  $A_jB_{-j}$  in the same manner. All of these correlations reduce in the way demonstrated here, and thus equation (5) can indeed be treated as a random walk on the complex plane.

## APPENDIX B: CROSS-SPECTRUM CALCULATION

The mass accretion rate in the  $l$ th ring is

$$\dot{m}(r_l, t) = \prod_{q=1}^l (\tilde{a}_q(t - \Delta t_{ql}) + \mu_q), \quad (\text{B1})$$

where a tilde denotes zero mean. We can write this as

$$\dot{m}(r_l, t) = \sum_{\theta} \prod_{q=1}^l \theta_{ql}, \quad (\text{B2})$$

where  $\theta_{ql}$  can either be  $\mu_q$  or  $\tilde{a}_q(t - \Delta t_{ql})$  and the sum is over every combination (i.e. not permutation) of  $\theta$ . For example, for the third ring we have

$$\dot{m}(r_3, t) = \tilde{a}_1(t - \Delta t_{13})\tilde{a}_2(t - \Delta t_{23})\tilde{a}_3(t) \\ + \mu_1\tilde{a}_2(t - \Delta t_{23})\tilde{a}_3(t) + \mu_2\tilde{a}_1(t - \Delta t_{13})\tilde{a}_3(t) \\ + \mu_3\tilde{a}_1(t - \Delta t_{13})\tilde{a}_2(t - \Delta t_{23}) + \mu_1\mu_2\tilde{a}_3(t) \\ + \mu_1\mu_3\tilde{a}_2(t - \Delta t_{23}) + \mu_2\mu_3\tilde{a}_1(t - \Delta t_{13}) \\ + \mu_1\mu_2\mu_3, \quad (\text{B3})$$

and so each term is a product of  $l = 3$  terms and the sum is over every different combination that triplet can take. We can use this to know which terms correlate between the  $n$ th and  $l$ th ring because the mass accretion rate in the  $n$ th ring is

$$\dot{m}(r_n, t) = \sum_{\theta} \prod_{q=l+1}^n \theta_{qn} \prod_{q=1}^l \theta_{qn} \\ = \prod_{q=l+1}^n \mu_q \sum_{\theta} \prod_{q=1}^l \theta_{qn} + \text{uncorrelated terms.}$$

We know that  $\theta_{qn}$  represents either  $\mu_q$  or  $\tilde{a}_q(t - \Delta t_{qn})$ . In the former case, it is easy to see that  $\theta_{qn} = \theta_{ql}$  (i.e.  $\mu_q = \mu_q$ ). The latter case is a little more complicated but we can use the definition of  $\Delta t_{ln}$  (equation 13) in order to show that  $\tilde{a}_q(t - \Delta t_{qn}) = \tilde{a}_q(t - \Delta t_{ql} - \Delta t_{ln})$  and thus

$$\dot{m}(r_n, t) = \Lambda_{ln}\dot{m}(r_l, t - \Delta t_{ln}) + \text{uncorrelated terms.} \quad (\text{B4})$$

From here it is simple to show that equation (19) is true.

This paper has been typeset from a  $\text{\LaTeX}$  file prepared by the author.